Research Square

Preprints are preliminary reports that have not undergone peer review.
They should not be considered conclusive, used to inform clinical practice,
or referenced by the media as validated information.

WITHDRAWN: Amorphizing noble metal for single-atom-layer catalysis

Yongmin He
Nanyang Technological University https://orcid.org/0000-0002-9347-930X
Liren Liu
College of Aerospace Engineering, Nanjing University of Aeronautics and Astronautics
Chao Zhu
Nanyang Technological University https://orcid.org/0000-0001-6383-3665
Prafful Golani
Nanyang Technological University
Bonhyeong Koo
Deparment of Materials Science and Engineering, Korea Advanced Institute of Science and Technology
Shasha Guo
Nanyang Technological University
Pengyi Tang
Ernst Ruska-Centre for Microscopy and Spectroscopy with Electrons https://orcid.org/0000-0002-2306-095X
Zhiqiang Zhao
College of Aerospace Engineering, Nanjing University of Aeronautics and Astronautics
Manzhang Xu
Nanyang Technological University https://orcid.org/0000-0001-6752-5299
Chao Zhu
Nanyang Technological University https://orcid.org/0000-0002-1589-855X
Peng Yu
Sun Yat-sen University
Xuewen Wang
Northwestern Polytechnical University https://orcid.org/0000-0002-9689-6678
Lu Zheng
Xi'an Key Laboratory of Flexible Electronics (KLoFE), NorthwesternPolytechnical University
Jiefu Yang
School of Materials Science and Engineering, Nanyang Technological University
Byungha Shin
Korea Advanced Institute of Science and Technology https://orcid.org/0000-0001-6845-0305
Jordi Arbiol

Catalan Institute of Nanoscience and Nanotechnology (ICN2), CSIC and BIST, Campus UAB, Bellaterra, 08193 Barcelona, Catalonia, Spain https://orcid.org/0000-0002-0695-1726

Qi Jie Wang

Nanyang Technological University https://orcid.org/0000-0002-9910-1455

Zhuhua Zhang

Nanjing University of Aeronautics and Astronautics https://orcid.org/0000-0001-6406-0959

Zheng Liu

z.liu@ntu.edu.sg

Nanyang Technological University https://orcid.org/0000-0002-8825-7198

Article

Keywords: Noble Catalysts, Industrial Applications, Atom-utilization Efficiency, Sustained High-flux Hydrogen, Amorphization Strategy

Posted Date: December 12th, 2020

DOI: https://doi.org/10.21203/rs.3.rs-122389/v1

License: This work is licensed under a Creative Commons Attribution 4.0 International License. Read Full License

Additional Declarations: There is **NO** Competing Interest.

EDITORIAL NOTE:

The full text of this preprint has been withdrawn by the authors while they make corrections to the work. Therefore, the authors do not wish this work to be cited as a reference. Questions should be directed to the corresponding author.

Abstract

Rational design of noble catalysts with a potential to leverage efficiency at the atomic scale is vital for industrial applications. Such an ultimate atom-utilization efficiency can be achieved when all noble atoms exclusively contribute to catalysis. Here, we demonstrate a scalable synthesis of freestanding amorphous $PtSe_x$ (where $1.2 < x < 1.3$) layers acting as single-atom-layer of Pt catalysts with an unprecedentedly high atom-utilization efficiency (~ 30 wt%) at the monolayer limit. The amorphous $PtSe_x$ behaviors a fully-activated surface accessible to catalytic reactions. The catalytic performance of the amorphous layer is featured by a nearly 100% current density relative to a pure Pt surface and reliable production of sustained high-flux hydrogen over a 2-inch sized wafer sample as a proof-of-concept. Furthermore, an electrolyser using the $PtSe_x$ amorphous layer as a cathode is demonstrated to generate a high current density of 1000 mA cm^{-2}. Such an amorphization strategy is potentially extendable to other noble metals, including Pd, Ir, Os, Rh, and Ru elements, demonstrating the universality of single-atom-layer catalysts.

Introduction

The high cost of noble metal sources, represented by Platinum (Pt) and Palladium (Pd), has hindered the broad deployment of fuel cells and metal-air batteries for commercial applications towards a sustainable energy storage area.[1] Taking Auto System market for an example, the usage of the total Pt content in fuel cell was about 0.117 g/kWgross in 2018, will be cut down to 0.108 g/kWgross in 2020 and as low as 0.064 g/kWgross in 2025 for the cost demand.[2] In order to reduce the cost, noble metals have been engineered into various nanostructured catalysts,[3,4] including 3D porous structures[5], 2D nanosheets[6,7], 1D nanowires[8,9], 0D clusters (Figure 1a), or even as small as individual atoms (Figure 1b).[10-12] Such a trend will evolve into an ultimate landscape of the noble metal atoms at the monolayer limit (for thickness <1 nm), that is, single-atom-layer catalysis (Figure 1c), wherein nearly all the atoms are reconfigurable for a maximum density while being accessible to catalytic reactions, capable of electrocatalytic activities and stable thermodynamically.

In this work, we have demonstrated the synthesis of single-atom-layer catalysis, exampled by atom-thin amorphous $PtSe_x$ as an HER electrocatalyst and its potential as an alternative to platinum (Figure 1c). First, we report the synthesis of wafer-scale, one-nanometer-thick $PtSe_x$ layer with amorphous yet robust structures through ion etching of pre-deposited 2D $PtSe_2$ under a low-density Ar plasma at a temperature of -30 ^oC. The loss of Selenium (Se) atoms in the amorphous layer yields a stable Pt single-atom-layer phase on its surface, as evidenced by complementary characterizations, including atomic resolution aberration-corrected (AC) high angle annular dark-field (HAADF) scanning transmission electron microscopy (STEM), Raman and X-ray absorption fine structure (XAFS) spectroscopy, electrical measurements, and supported by intensive first-principles calculations. Next, our micro-electrochemical cell measurement shows that the amorphous $PtSe_x$ layer exhibits as excellent catalytic performance as that of a pure Pt surface with onset potential of 0 V, Tafel slope of 39 mV dec^{-1}, and current density of 25

mA cm^{-2} at a low potential of 50 mV. The utility of the wafer-scale amorphous $PtSe_x$ layer was further demonstrated with an electrolyzer, showing sustainable, mass production of hydrogen. These results have opened a way to optimized catalytic performance of 2D and similar materials based on amorphization.

Results

Fabrication of atomically thin amorphous $PtSe_x$

We used low-temperature deep reactive ion etching (DRIE) with a low-density Argon (Ar) plasma to convert the atomically-thin crystalline $PtSe_2$ (1T phase) film into an amorphous $PtSe_x$ film. First, a 2-inch wafer-size $PtSe_2$ film with a ~0.6 nm thickness was prepared through a two-step selenylation of Pt metal on a SiO_2/Si substrate (explained in Supplementary Figure S1). Then, the as-grown film was etched by DRIE at a low-temperature of -30 ^oC for 50 seconds to obtain the amorphous $PtSe_x$ layer ($1.2<x<1.3$). Figure 1d shows a ~1-nm thickness and wafer-scale $PtSe_x$ film on a SiO_2/Si substrate. With a wet transfer method (as reported in Supplementary Figure S2), a uniform and continuous film was suspended on a Cu-supported lacey carbon transmission electron microscopy (TEM) grid, as shown in Figure 1e.

In order to characterize the synthesized $PtSe_x$, we conducted atomic-resolution high-angle annular darkfield (HAADF) imaging *via* the STEM (Figures 1f-g and Supplementary Figures S3-S4). The dark-field images of the $PtSe_x$ film show a random distribution of the Pt atoms (bright spots in the image) in the film (Figure 1g). Interestingly, there is no long-range order in the atomic arrangement, indicating that the achieved film is amorphous. Moreover, the typical FFT spectrum (a 20×20 nm^2 area) has a broad and continuous halo (Figure 1f) with no diffraction spots, which better visualizes a complete amorphization through an area of nearly 4000 nm^2 (Supplementary Figure S3). Next, we randomly chose five regions in the $PtSe_x$ film, whose STEM images showed a uniform amorphization process over a large-scale (Supplementary Figure S4). This amorphization process is also verified by Raman spectra, which exhibit nearly negligible characteristic peaks (E_g and A_{1g}) compared to the crystalline $PtSe_2$ film (Figure 1h). Different from previously reported carbon amorphous monolayers[13] (0.6 nm thickness), our amorphous $PtSe_x$ layer is made of Pt and Se atoms with more complicated coordination and, to the best of our knowledge, is the first binary amorphous layer. Notably, our amorphous layer can be thermodynamically stable in a 2D form with a thickness down to 1 nm. Such a highly stable, ultrathin amorphous layer has been long sought, since it can expose nearly all the Pt atoms to electrocatalysis, as will be discussed later.

The formation of the amorphous layer is largely attributed to the low-temperature processing and the low-density Ar plasma. The low-temperature selenylation of Pt films avoids the solid-state dewetting behavior[14] to form a porous film (Supplementary Figure S5), and the low-temperature substrate (approximately -30 ^oC, during DRIE) suppresses the plasma-induced local heating that may cause aggregation of surface atoms and lead to incomplete amorphization (Supplementary Figure S6). The

low-density Ar plasma[15] drives the phase transition of $PtSe_x$ smoothly by adjusting the etching duration. During the DRIE process, the original film evolves from a crystalline 1T phase ($PtSe_2$), via a defected-1T phase and then a mixture of amorphous structure/1T phase ($PtSe_{1.3<x<1.4}$), finally to a completely amorphous structure ($PtSe_{1.2<x<1.3}$), as shown in Supplementary Figure S7.

We further performed XPS and electrical measurements on the amorphous $PtSe_x$, as shown in Figures 1i and Supplementary Figures S8-S9, respectively. In Pt 4f region, Pt(IV) and Pt(II) are observed, while no significant Pt(0) peaks are found. These XPS data at Pt 4f confirm that the amorphous $PtSe_x$ is a Pt-Se compound but not isolated Pt and Se nanoparticles, consistent with our STEM observations. Moreover, the back-gate electrical measurements (Figure 1j) shows that the amorphous $PtSe_x$ exhibits a high conductance (a resistivity of ~0.03 Ω mm) and no gating effect (inset of Figure 1j), in contrast to a p-type semiconducting behavior of crystalline $PtSe_2$. This result suggests an amorphization-induced metallization of the $PtSe_x$ layer.

Formation mechanism of the amorphous $PtSe_x$

We then performed *ab initio* calculations to understand the formation mechanism of amorphous $PtSe_x$ (see Methods section). To mimic the loss of Se atoms induced by ion etching, Se atoms were removed sequentially from a perfect single-crystal $PtSe_2$ while ensuring that the removed atom at each step is the one that costs minimum energy. Note that our calculations do not consider a real amorphous structure but aim to shed light on the local structural evolution induced by DRIE. To quantify the structural-deformation degree of $PtSe_x$ induced by the Se removal, we define a parameter based on the displacement of Pt atoms, δ_{Pt}, expressed by $\delta_{Pt} = |P_i - P_i^0|$ with $i = 1, 2, \ldots N$, where N is the total number of Pt atoms in the supercell, P_i and P_i^0 are the positions of i^{th} Pt atom in the $PtSe_x$ and perfect single-crystal $PtSe_2$, respectively. Then, an averaged displacement of Pt is given by $\langle\delta_{Pt}\rangle = \Sigma|P_i - P_i^0|/N$. The sequential Se removal yields a distinct vacancy order in the film, in which each Se vacancy connects to its neighbors with four-coordinated Pt atoms (Figure 2a, top). However, the 1T framework of defective $PtSe_x$ is barely distorted even when x decreases to 1.5, as supported by calculated δ_{Pt} and $\langle\delta_{Pt}\rangle$ shown at the bottom of Figure 2a. These results suggest that the crystalline structure of $PtSe_x$ (*i.e.,* $1.5<x<2$) is rather robust to short-term ion-etching, in line with our experimental results.

Further decreasing the ratio of Se ($x<1.5$) leads to three-coordinated Pt atoms. Every two of these three-coordinated Pt atoms, resulting from a single Se removal, shift towards each other to stabilize the 2D $PtSe_x$ (see circles in Figure 2a), then severely disturbing the local bond networks. However, the overall structure remains essentially crystalline if the three-coordinated Pt atoms are insufficiently dense (Figure 2a). In our calculations, both relaxed structures and calculated $\langle\delta_{Pt}\rangle$ suggest that the local amorphization starts at a Se/Pt ratio of ~1.38, and a complete amorphization occurs at a ratio of 1.33 with $\langle\delta_{Pt}\rangle$ exceeding 1.0 Å (Figures 2a, 2b and Figures S10-S16, respectively). The amorphization roots in the randomness of creating three-coordinated Pt atoms across the whole layer. For the amorphous $PtSe_{1.33}$,

we already cannot find long-range lattice order within our supercell. The general trend of amorphization agrees with our experimental observation (Supplementary Figure S7). Further decreasing x in 2D $PtSe_x$ enhances the amorphous characteristic, as evidenced by relaxed structures of $PtSe_{1.33}$, $PtSe_{1.30}$, $PtSe_{1.27}$, and $PtSe_{1.25}$ (Figures 2a and b).

Experimentally, the detailed amorphous structure is analyzed by mapping the precise position of Pt atoms in $PtSe_x$ based on our STEM imaging (Figure 2c), which then allowed us to determine the projected distances between two adjacent Pt atoms onto the basal plane. The data for a perfect $PtSe_2$ sheet is taken as a reference. It turns out that the projected Pt-Pt distances in the amorphous $PtSe_{1.33}$ are peaked at ideal 3.73 Å but exhibit a much broader distribution over 3.0–4.5 Å than those in a perfect $PtSe_2$ (Figure 2d and Supplementary Figure S17). These distances agree well with our *ab initio* molecular dynamics calculations in terms of the broad distribution and the peak position (Figure 2d), so does the Pt-Se bond angles in the 2D $PtSe_x$ (Supplementary Figures S18). Such a broad distribution of the bond geometry also echoes the results in the reported amorphous carbon monolayers[13] and O–Si–O bonds in a silica bilayer[16], featuring a 2D amorphous network without long-ranged order.

Catalytic activity of amorphous $PtSe_x$

The hydrogen evolution reaction (HER) activity of the amorphous $PtSe_x$ is tested using micro-electrochemical cells[17,18], as shown in Figure 3a and Supplementary Figure S19. Starting from the same mechanically exfoliated $PtSe_2$ nanosheet, we etched different regions at controlled duration, and obtained regions of perfect single-crystal, defective single-crystal, and amorphous $PtSe_x$ (Supplementary Figure S20) for comparing their HER activities. The electrocatalytic performance of these regions are summarized in Figure 3b and Supplementary Figures S21: (1) The basal plane of perfect single-crystal is HER-inert, as has been widely measured[15,19]. (2) At the initial stage of the plasma etching, only isolated Se vacancies are created as active sites, yielding a moderate HER performance (onset potential: ~0.1 V and Tafel slope: ~100 mV dec^{-1}); an increased number of Se vacancies results in an enhanced HER performance. (3) As the treatment continues, amorphous $PtSe_x$ is formed and exhibits excellent catalytic performance, e.g. onset potential of 0V, Tafel slope of 39 mV dec^{-1}, and current density of 25 mA cm^{-2} at 50 mV for the $PtSe_{1.26}$. An abruptly-improved performance is observed during this process due to the transition of the catalytic site, *that is*, from Se vacancies to amorphous Pt site. In order to elaborate the evolution of active sites, we tested tens of $PtSe_x$ nanosheets, and plotted their onset potentials and Tafel slopes versus Se/Pt atom ratio in Figure 3c, which confirms our conclusion above.

It is compelling to see that the amorphous $PtSe_x$ offers comparable catalytic performance to pure Pt, which is feature by onset potential: 0V, Tafel slope: 37 mV dec^{-1}, and current density: 25 mA cm^{-2} at 50 mV (Figures 3d and 3e). The Tafel curves shown in Figure 3e reveal a similar rate-limiting step for the reaction kinetics between the amorphous $PtSe_x$ and pure Pt[20], which renders the amorphous $PtSe_x$ with a Pt-like catalytic characteristic. More importantly, the nearly 100% current density indicates a maximal

density of active sites enabled by the amorphous structure (Figure 3f). This ratio, to the best of our knowledge, is record-high in current TMD catalysts, especially in light of that the current density is less than 1% in PtX_2 (X=S, Se, Te) and other TMDs and ranged between 4-55% in metallic VS_2, VSe_2, NbS_2, $Nb_{1.35}S_2$, and TaS_2 catalysts (see Supplementary Figure S22 and Table S1 for comparison).

To gain further insight into the electrocatalytic performance of amorphous $PtSe_x$, we calculated Gibbs free energy of adsorbed hydrogen atoms (ΔG_H) by scanning all possible sites on the surface of an amorphous $PtSe_{1.33}$. Since the amorphous $PtSe_x$ layer may provide a layer of Pt sites with different reactivities, taking the hydrogen coverage into account is necessary to evaluate the catalytic activity of the whole layer. The hydrogen coverage[21,22] is defined as , where N_H is the number of hydrogen atoms and M_{Pt} is the total number of Pt sites (Supplementary Figures S23-32). The hydrogen coverage varies from 2.8% to 27.8 %. Unlike Pt in single-atom catalysts (*e.g.*, Pt-doped in TMDs[23] and graphene[12]), the Pt atoms with diverse bond geometries in the amorphous $PtSe_x$ yield a wide range of ΔG_H shown in Figure 3g. If the sites with ΔG (eV) falling in the range (-0.3, 0.3) are considered active, ~ 30% Pt atoms could contribute to the HER at a hydrogen coverage of 28%. Such an unusual high-density of active sites is attributed to three-coordinated Pt atoms that give rise to a high density of states of 5d orbitals near the Fermi level (Supplementary Figure S33). This density sustains across hydrogen coverages from 5.6%-28% (Figure 3g). Based on the calculations, we can estimate an atom-utilization efficiency of Pt atoms of up to ~30 wt% in the amorphous $PtSe_x$, much higher than ~5 wt% in previously proposed single-atom Pt catalysts[4]. Such a high atom-utilization efficiency explains why the amorphous $PtSe_x$ can deliver a nearly 100% current density relative to the pure Pt metal (Figures 3d-f). Thus, we coin the amorphous $PtSe_x$ as single-atom-layer catalyst (Figure 3h), a new type of Pt catalyst that is superior to the widely studied single-atom and defect-enabled catalysts.

Stability and large-scale hydrogen production of amorphous $PtSe_x$ catalyst

As a proof-of-concept for hydrogen generation, the 2-inch amorphous $PtSe_x$ layer is transferred onto an Au substrate for mass production of hydrogen. Figure 4a shows a large amount of hydrogen bubbles produced from this catalyst (also see Supplementary Figure 34 and Movie 1). We further examine the catalytic stability of amorphous $PtSe_x$. The polarization curve has negligible loss of the cathodic current after 10,000 potential cycles (Figure 4b). The Tafel slopes after cycles persist as their initial states (see inset of Figure 4b). Furthermore, the chrono-potentiometric test (overpotential versus time) conducted for 100 hours shows that this amorphous $PtSe_x$ also possesses long-term stability at both small and large current densities, *i.e.* 20 and 140 mA cm^{-2}, respectively (Figure 4c).

We also made a two-electrode electrolyser cell for overall water splitting. Figure 4d shows a photograph of an assembled full-cell consisting of an amorphous $PtSe_x$ layer on a FTO substrate as a cathode and an IrO_x film as an anode. The reaction initially has a low onset potential of 1.25 V (see the inset of Figure 4e), close to the theoretical voltage limit (1.23 V). Meanwhile, the current density of this electrolyser is as

high as 250 mA cm^{-2} at 1.7 V, and later reaches up to 1000 mA cm^{-2}, as shown in Figure 4e and Supplementary Movie 2. These parameters are superior to the reported electrolysers based on thin 2D materials with a current density of 10-100 mA cm^{-2} at similar reaction potentials[24], and are even close to those of industrial Pt and Ir electrolysers (~ 1000 mA cm^{-2})[25,26]. In real applications, the loss or deactivation of noble metal catalysts remains a major issue. To address this issue, we developed a "layer-by-layer replenishment" method of amorphous $PtSe_x$ using a controlled etching (Supplementary Figures 35-36). Once the old amorphous $PtSe_x$ layer becomes catalytically inactive, a new amorphous layer will be replenished. Such a process persists at least to the sixth new layer without obvious decay in current densities and Tafel slopes, suggesting a successful "replenishment".

Figure 5a presents a general approach to achieve amorphous noble MX_x libraries (M=Pt, Pd, Ir, Os, Ru, Rh; X=S, Se) via defect engineering. As the defect concentration increases, the original lattice structure is increasingly distorted. The as-produced amorphous MX_x would be stable in air due to the inert nature of noble metals, as demonstrated by $PtSe_x$ in our work. Indeed, our high-throughput *ab initio* molecular dynamics calculations suggested that all other noble metal selenide layers, such as $PdSe_2$, $IrSe_2$, $OsSe_2$, $RuSe_2$ and $RhSe_2$, form stable amorphous layers as well (Figure 5b and Supplementary Figure 37). Notably, our preliminary experiments have realized a stable amorphous $PdSe_x$ layer (Supplementary Figures 38-39). In contrast, most non-noble metal (Mo, W, Re, etc)-based MX_x are unstable or even decompose in air due to the corrosion and oxidation of exposed metal atoms (see MoS_2 as an example in Figure 5a and Supplementary Figure 40).

Conclusions

We have realized the wafer-size synthesis of highly stable amorphous layer of noble metal chalcogenides, as exemplified by amorphous $PtSe_x$, by Ar plasma etching of pristine noble metal dichalcogenides at low temperatures, and disclosed the transition mechanism of amorphous $PtSe_x$ from perfect $PtSe_2$. This amorphous $PtSe_x$ layer of ~1 nm thickness provides a robust single-layer of noble metal atoms that exhibits electrocatalytic performance rivaling that of pure noble metals, along with an unprecedentedly high atom-utilization efficiency. A two-electrode electrolyser cell made of $PtSe_x$ as cathode and IrO_x as anode has delivered promising overall water splitting performance compared to existing 2D materials-based devices. Beyond the $PtSe_x$ material, our work also opens opportunities to design a family of noble metal single-atom-layer catalysts from their amorphous selenides, such as $PdSe_x$, $IrSe_x$, $OsSe_x$, $RuSe_x$ and $RhSe_x$, boosting great potentials for various electrocatalytic applications.

Declarations

Acknowledgements

This work was supported by the Singapore National Research Foundation Singapore programme NRF-CRP21-2018-0007 and NRF-CRP22-2019-0060, Singapore Ministry of Education via AcRF Tier 3 (MOE2018-T3-1-002), AcRF Tier 2 (MOE2017-T2-2-136 and MOE2019-T2-2-105), and AcRF Tier 1 (RG7/18 and 2019-T1-002-034). This work was also supported by the National Natural Science Foundation of China (11772153), the Natural Science Foundation of Jiangsu Province (BK20190018), the Fundamental Research Funds for Central Universities (NE2018002, NJ2020003). This research was supported by the Singapore National Research Foundation Singapore programme NRF-CRP18-2017-02 and NRF–CRP19–2017–01, and Singapore Ministry of Education Tier 2 grant (MOE2018-T2-1-176).

Author Contributions

Z.L. and Y.H. conceived and initiated the project. Z.L. and Z.Z.(Dr.) supervised the project and led the collaboration efforts. Y.H. designed the experiments, synthesized $PtSe_x$ films, and performed micro/macro-electrochemical HER measurement. C.Z., P.T., and J.A. performed the TEM and STEM measurements. Z.Z.(Dr.), L.L., and Z.Z.(Mr) performed the first-principles calculations and theoretical calculation of ΔG_H. B.K. and B.S. did the electrolyzer-cell measurement. P.G., S.G., M.X., X.W., L.Z., and J.Y. assisted material characterizations and CVD synthesis. P.Y. helped the synthesis of $PtSe_2$ single crystal by the CVT method. Y.H., L.L., Q.W., Z.Z.(Dr.) and Z.L. wrote the paper. All authors discussed the results and commented on the manuscript.

Competing interests

The authors declare no conflict of interest.

Additional information

Correspondence and requests for materials should be addressed to Q.W., Z.Z., and Z.L.

References

1 Chao, W. *et al.* Cations in Octahedral Sites: A Descriptor for Oxygen Electrocatalysis on Transition-Metal Spinels. *Adv. Mater.* **29**, 1606800 (2017).

2 James, B. 2018 Cost Projections of PEM Fuel Cell Systems for Automobiles and Medium-Duty Vehicles. (2018).

3 Liu, M., Zhao, Z., Duan, X. & Huang, Y. Nanoscale Structure Design for High-Performance Pt-Based ORR Catalysts. *Adv. Mater.* **31**, 1802234 (2019).

4 Zhang, L., Doyle-Davis, K. & Sun, X. Pt-Based electrocatalysts with high atom utilization efficiency: from nanostructures to single atoms. *Energy Environ. Sci.* **12**, 492-517 (2019).

5 Xu, Y. & Zhang, B. Recent advances in porous Pt-based nanostructures: synthesis and electrochemical applications. *Chem. Soc. Rev.* **43**, 2439-2450 (2014).

6 Funatsu, A. *et al.* Synthesis of monolayer platinum nanosheets. *Chem. Commun.* **50**, 8503-8506 (2014).

7 Kijima, T. *et al.* Synthesis of Nanohole-Structured Single-Crystalline Platinum Nanosheets Using Surfactant-Liquid-Crystals and their Electrochemical Characterization. *Adv. Funct. Mater.* **19**, 545-553 (2009).

8 Yin, H. *et al.* Ultrathin platinum nanowires grown on single-layered nickel hydroxide with high hydrogen evolution activity. *Nat. Commun.* **6**, 6430 (2015).

9 Li, M. *et al.* Ultrafine jagged platinum nanowires enable ultrahigh mass activity for the oxygen reduction reaction. *Science* **354**, 1414-1419 (2016).

10 Chen, C. *et al.* Highly Crystalline Multimetallic Nanoframes with Three-Dimensional Electrocatalytic Surfaces. *Science* **343**, 1339-1343 (2014).

11 Zhao, M. *et al.* Metal–organic frameworks as selectivity regulators for hydrogenation reactions. *Nature* **539**, 76 (2016).

12 Cheng, N. *et al.* Platinum single-atom and cluster catalysis of the hydrogen evolution reaction. *Nat. Commun.* **7**, 13638 (2016).

13 Toh, C.-T. *et al.* Synthesis and properties of free-standing monolayer amorphous carbon. *Nature* **577**, 199-203 (2020).

14 Lee, S.-H., Kwak, E.-H. & Jeong, G.-H. Dewetting behavior of electron-beam-deposited Au thin films on various substrates: graphenes, quartz, and SiO_2 wafers. *Appl. Phys. A* **118**, 389-396 (2015).

15 Li, H. *et al.* Activating and optimizing MoS_2 basal planes for hydrogen evolution through the formation of strained sulphur vacancies. *Nat. Mater.* **15**, 48-53 (2016).

16 Lichtenstein, L. *et al.* The Atomic Structure of a Metal-Supported Vitreous Thin Silica Film. *Angew. Chem. Int. Ed.* **51**, 404-407 (2012).

17 He, Y. *et al.* Self-gating in semiconductor electrocatalysis. *Nat. Mater.* **18**, 1098-1104 (2019).

18 He, Y. *et al.* Engineering grain boundaries at the 2D limit for the hydrogen evolution reaction. *Nat. Commun.* **11**, 57 (2020).

19 Jaramillo, T. F. *et al.* Identification of active edge sites for electrochemical H_2 evolution from MoS_2 nanocatalysts. *Science* **317**, 100-102 (2007).

20 Li, Y. *et al.* MoS_2 nanoparticles grown on graphene: an advanced catalyst for the hydrogen evolution reaction. *J. Am. Chem. Soc.* **133**, 7296-7299 (2011).

21 Wang, T. *et al.* High Coverage CO Activation Mechanisms on Fe(100) from Computations. *J. Phys. Chem. C* **118**, 1095-1101 (2014).

22 Digne, M., Sautet, P., Raybaud, P., Euzen, P. & Toulhoat, H. Use of DFT to achieve a rational understanding of acid–basic properties of γ-alumina surfaces. *J. Catal.* **226**, 54-68 (2004).

23 Li, H. *et al.* Synergetic interaction between neighbouring platinum monomers in CO_2 hydrogenation. *Nat. Nanotechnol.* **13**, 411-417 (2018).

24 Han, N. *et al.* Nitrogen-doped tungsten carbide nanoarray as an efficient bifunctional electrocatalyst for water splitting in acid. *Nat. Commun.* **9**, 924 (2018).

25 Zhigang, S., Baolian, Y. & Ming, H. Bifunctional electrodes with a thin catalyst layer for `unitized' proton exchange membrane regenerative fuel cell. *J. Power Sources* **79**, 82-85 (1999).

26 Altmann, S., Kaz, T. & Friedrich, K. A. Bifunctional electrodes for unitised regenerative fuel cells. *Electrochim. Acta* **56**, 4287-4293 (2011).

27 Perdew, J. P., Burke, K. & Ernzerhof, M. Generalized Gradient Approximation Made Simple. *Phys. Rev. Lett.* **78**, 1396-1396 (1997).

28 Hafner, J. Ab-initio simulations of materials using VASP: Density-functional theory and beyond. *J. Comput. Chem.* **29**, 2044-2078 (2008).

29 Kresse, G. & Joubert, D. From ultrasoft pseudopotentials to the projector augmented-wave method. *Phys. Rev. B* **59**, 1758-1775 (1999).

30 He, Q. *et al.* In Situ Probing Molecular Intercalation in Two-Dimensional Layered Semiconductors. *Nano Lett.* (2019).

31 Labrador, N. Y. *et al.* Enhanced Performance of Si MIS Photocathodes Containing Oxide-Coated Nanoparticle Electrocatalysts. *Nano Lett.* **16**, 6452-6459 (2016).

Materials And Methods

Fabrication of water-size $PtSe_x$ film.

There are three steps involved in the fabrication process: (i) Depositing a ~0.6 nm thick Pt layers on a clean 2-inch sapphire or SiO_2/Si wafer by e-beam evaporation at the rate of 0.1 Å s^{-1}. The deposition temperature of substrate is kept at room temperature to avoid the agglomeration of film; (ii) Selenizing those metal films in a CVD apparatus, which is depicted in detail in Figure S1. Selenium powder is loaded

in an Aluminum Oxide boat and placed both at the upstream and middle of tube, enabling a continuous supply of Selenium (Se) vapor sources. The selenylation temperature was first kept at 200 ^{o}C in low-vacuum conditions at 10-100 kPa for 1-2 hours, in which this low-temperature will avoid the solid-state dewetting behavior[14] to form a porous film (Figure S5), and then increased up to 550 ^{o}C to realize the complete selenylation. (iii) The samples were finally exposed to an Ar plasma atmosphere at a low temperature (approximately -30 ^{o}C) for various treatment durations. The low-density Ar plasma was generated by a deep reactive ion etching (DRIE) systems (Oxford PlasmaLab System 100) with a 5 W RF power in a vacuum chamber (10^{-3} torr of plasma pressure), which delivers the short mean free paths for the radicals in a plasma atmosphere. A low temperature substrate (approximately -30 ^{o}C) is to hinder the plasma-induced local heating during etching process (Figure S6), which would cause the aggregation of surface atom and a uncompleted amorphization.

First-principles calculations

The calculations were performed within the framework of density functional theory (DFT) with the Perdew-Burke-Ernzerh functional[27], as implemented in the Vienna Ab initio Simulation Package (VASP) code[28]. A vacuum space of 20 Å was set to eliminate spurious interaction between two $PtSe_x$ surfaces in adjacent periodic images. The core electron-ion interaction was described by the projector augmented wave potential[27,29], and the plane-wave basis set cutoff energy was set to be 450 eV. We simulated a bilayer $PtSe_2$ with a 15×15 supercell, in which the atoms of the bottom layer were fixed while those in the top layer were allowed to relax. The Brillouin zone integration was sampled using 4×4×1 k-points for the structural optimization and 2×2×1 k-points for molecular dynamics (MD) simulations. The atomic positions were optimized until the maximum force on each atom was less than 0.01 eV/Å. The NVT ensemble was used for MD simulations.

For every isomer structure of $PtSe_x$, the thermal stabilities at high temperatures are studied using ab initio molecule dynamics (MD) simulations. First, all structures of $PtSe_x$ were relaxed in MD simulations for 5 picoseconds at 1000 K, and then each structure was geometrically optimized at 0 K. Finally, the thermal stability of all optimized structures were re-examined by 5 picoseconds MD simulation at 800 K. By removing Se atoms from the $PtSe_2$ crystal surface, the structures of $PtSe_2$ crystal with $PtSe_x$ surface can be obtained. Every single structure of $PtSe_x$ (x=2,1.8,1.6,…,1) is optimized firstly to ensure it has lower energy, and then fully relaxed by molecular dynamics method to ensure it's stability. Considering the effect of Ar plasma on the $PtSe_x$ surface, the stone-wales defect in $PtSe_x$ is considered to certain extent.

Theoretical calculation of ΔG_H

The *ab initio* calculations were also implemented by using PBE-GGA method in the VASP code. A kinetic energy cutoff was set to 500 eV for the plane-wave expansion, and a vacuum region of 15 Å was adopted to isolate neighboring periodic images. Brillouin-zone integration was sampled with 4 k-points for

relaxation and 16 k-points for electronic calculations. The positions of all the atoms were relaxed using the conjugate-gradient method until the force on each atom was less than 0.01 eV/Å.

The Gibbs free energies ΔG_H at 300 K were calculated with:

$$\Delta G = \Delta E + \Delta E_{ZPE} - T\Delta S_H \quad (1)$$

$$\Delta E = E_{surf+nH} - E_{surf+(n-1)H} - {}^1/_2 E_{H_2} \quad n = 1,2,3... \quad (2)$$

$$\Delta E_{ZPE} - T\Delta S_H = 0.173eV \quad (3)$$

Where T is the temperature, ΔS_H is the entropy of an H atom adsorbed on $PtSe_x$ substrate, $E_{surf+nH}$ is the energy of $PtSe_x$ substrate with *n* hydrogen atoms and is the energy of free hydrogen molecule, ΔE_{ZPE} is the zero-point vibrational energy. The harmonic approximation limited is employed for the vibrational analysis of adsorbates, while gas phase reference molecules are treated as ideal.

Fabrication of micro-devices

(i) Fabrication of $PtSe_2$ nanosheet based micro-device. First, 16×16 mm SiO_2 (285 nm)/Si chips with pre-patterned 32 Au contact pads were fabricated using photolithography. Second, mechanically-exfoliated $PtSe_2$ nanosheets were transferred onto the chips. Third, the metal electrodes were made on the nanosheet by electron-beam lithography (EBL) followed by thermal or electron-beam evaporation of 5/60 nm Cr/Au. Finally, the device chip was passivated with 500 nm poly(methylmethacrylate) (PMMA) film, followed by EBL process to create the window on the PMMA to expose the region of interest on the nanosheet (d_1-d_N). As the PMMA is inert in the potential range investigated, we expect the electrochemical reactions only occur on the exposed regions. Note that, we choose the mechanically-exfoliated $PtSe_2$ nanosheet due to its perfect atomic surface, which can guarantee that no other activity sites (defects or edges) can make the interferences on the measurement. The reaction windows were opened at the desired regions on the same nanosheet with varied Ar-plasma treatment time. As a result, this micro-cell method allows a rigorous (or even semi-quantitative) investigation on the surface evolutions of $PtSe_2$ from 1T phase to amorphous.

(ii) Fabrication of 40 nm-thick Pt film based micro-device. In order to compare the electrocatalytic performance between Pt and amorphous $PtSe_{1.3}$ in micro-cell, we made a Pt microelectrode. A variety of Pt/Ti (40nm/2nm) nanostrips were fabricated onto the aforementioned pre-patterned chip by laser writing method followed by electron-beam evaporation of 2 nm Ti and 40 nm Pt. The bottom Ti layer employed here is served as an adhesion layer between Pt film and SiO_2/Si substrate. Same as the above micro-cell device, a reaction window was opened on PMMA passivation film by EBL to expose Pt film for HER measurement.

Micro-electrochemical measurement

A micro-electrochemical measurement[17,30] was employed in our work. Among the four electrodes, two were connected to graphite (high-purity) and Ag/AgCl micro reference electrode (Harvard Apparatus) to function as the counter and reference respectively. The other two electrodes were connected to the $PtSe_x$ nanosheets as drain and source contacts to collect their conductive and electrocatalytic signals during HER process. In all experiments, only the exposed region of nanosheets contributes to the electrocatalytic performance, and the rest of area in contact with electrolyte were passivated using PMMA film. During a micro-cell measurement, the scan rate of electrochemical potential is 10 mV/step. The electrocatalytic current density was calculated by normalizing the current to the open area of PMMA on the nanosheets. In this work, we express the electrochemical reference voltage with respect to RHE, given by

$$E_{RHE} = E_{Ag/AgCl} + 0.219\ V \qquad (4)$$

Macro-electrochemical measurements

The macro-electrochemical measurements were conducted on a glassy-carbon electrode (3 mm in diameter), in which the top of rod (electrode surface) can be screwed off to facilitate the operation. Using a similar PMMA-assist transfer method as described above, we transferred an 0.5×0.5 cm^2 amorphous $PtSe_x$ layer, which is made from CVD-grown $PtSe_2$, on a glassy carbon electrode (3 mm in diameter), and the sample area exceeding to glassy carbon electrode was scraped off before measuments. A standard three-electrode cell was used, where a graphite (high-purity) rod and a Ag/AgCl electrode served as counter and reference electrode, respectively. The measurements were conducted on a biological electrochemical station in H_2-saturated 0.5 M H_2SO_4 solution. Linear sweep voltammetry (LSV) was conducted at a scan rate of 5 mV s^{-1}, and the onset potential is defined as the beginning potential of Tafel linear region. The stability tests were carried out by two methods: (i) take continuous potential cycling in the potential window of -0.151 to ~ 0.219 V (versus RHE) at a scan rate of 100 mV s^{-1}; (ii) perform time-dependent overpotential ( ) curve under j = 20 mA cm^{-2} and 140 mA cm^{-2} in 0.5 M H_2SO_4 aqueous solution. The current density was normalized by the geometric surface area of the electrode.

Two-electrode electrolyser cell measurements

(i) Preparation of IrO_x electrocatalyst: Titanium (Ti) plate with a size of 2.5 x 2.5 cm^2 was used as substrate to deposit Ir. Prior to deposition, Ti plate was ultrasonicated with acetone (3 min), isopropyl alcohol (3 min), and DI water (3 min) to remove organic and inorganic contaminants on the surface followed by N_2 blowing and drying. Then, Ti plate was immediately loaded to e-beam evaporator with a base pressure of mid-10^{-6} Torr. A 50 nm thick Ti was deposited as an adhesive layer and a 100 nm thick Ir was deposited with a fixed deposition rate of 1.0 Å/s. After deposition, Ir/Ti plate was connected with Sn-Cu wire and the edges were sealed by an epoxy (Hysol 9460). And then, Ir/Ti plate was immersed in 1M KOH solution for 1 hour followed by continuous oxygen bubble formation by chronoamperometry to change iridium to iridium oxide and/or iridium hydroxide.

(ii) Electrochemical full-cell measurement: A two-electrode set-up was used to demonstrate electrochemical full-cell measurement. A $PtSe_x$ on FTO substrate was used as a working electrode. Prior to measurement, solution-processed SiO_x was deposited on $PtSe_x$/FTO to promote the mechanical adhesion of wet-transferred $PtSe_x$ on FTO. A thin SiO_x with thicknesses of 2, 5, 10 nm was tested on $PtSe_x$/FTO and 5 nm thickness of SiO_x showed the best current-potential characteristics. Details of preparation can be found in reference[31]. After SiO_x formation, working electrode was connected with lead wire using Ag paste and edges were sealed by an epoxy (Hysol 9460) except an active area. An Ir/Ti electrocatalyst was used as a counter electrode. A working electrolyte was 0.5M H_2SO_4 for hydrogen evolution and 1M NaOH for oxygen evolution. An H-cell was used to carry out full-cell measurement. A 30 ml of aqueous electrolyte was filled in an individual cell and a bipolar membrane (FuelCellStore) was utilized to separate the catholyte and anolyte. Before measurement, both electrolytes were purged with Ar during 30 min to eliminate unknown gas species. A BiStat (Bio-Logic) was used to measure two-electrode full-cell measurement with the scan rate of 20 mV/s.

Material characterizations

The microstructures and morphologies based on amorphous $PtSe_x$ were characterized by optical microscopy, scanning electron microscopy (SEM, FEI 4200), Raman spectroscopy (WITec alpha300 R), micro-X-ray photoelectron spectroscopy (micro-XPS, KRATOS-AXIS NOVA), and Scanning Transmission Electron Microscopy (STEM, JEOL ARM-200F (S)TEM equipped with CEOS CESCOR aberration corrector). The STEM imaging was operated at 80 kV acceleration voltage and the beam was set up to a convergence semi-angle of 28-33 mrad. High Angle Annular Dark Field (HAADF) imaging with the acquisition semi-angle of 68-280 mrad was employed to produce atomically resolved images whose intensity is approximately proportional to the square of the average atomic number Z of the material under investigation. This chemically-sensitive ‘Z-contrast’ mode is ideally suited to directly identify the nature of individual atoms. All the atomic resolution HAADF STEM images presented here were filtered with a Wiener filter. Raman and XPS measurements were conducted on the mechanically-exfoliated single-layer $PtSe_2$ samples with varied plasma treatment time. The micro-electrochemical measurements were performed using two source meters (keithley 2400 and 2450), synchronized by the general purpose interface bus (GPIB) and the LabView script, allowing simultaneous recording of the electronic and the electrochemical signals.

Figures

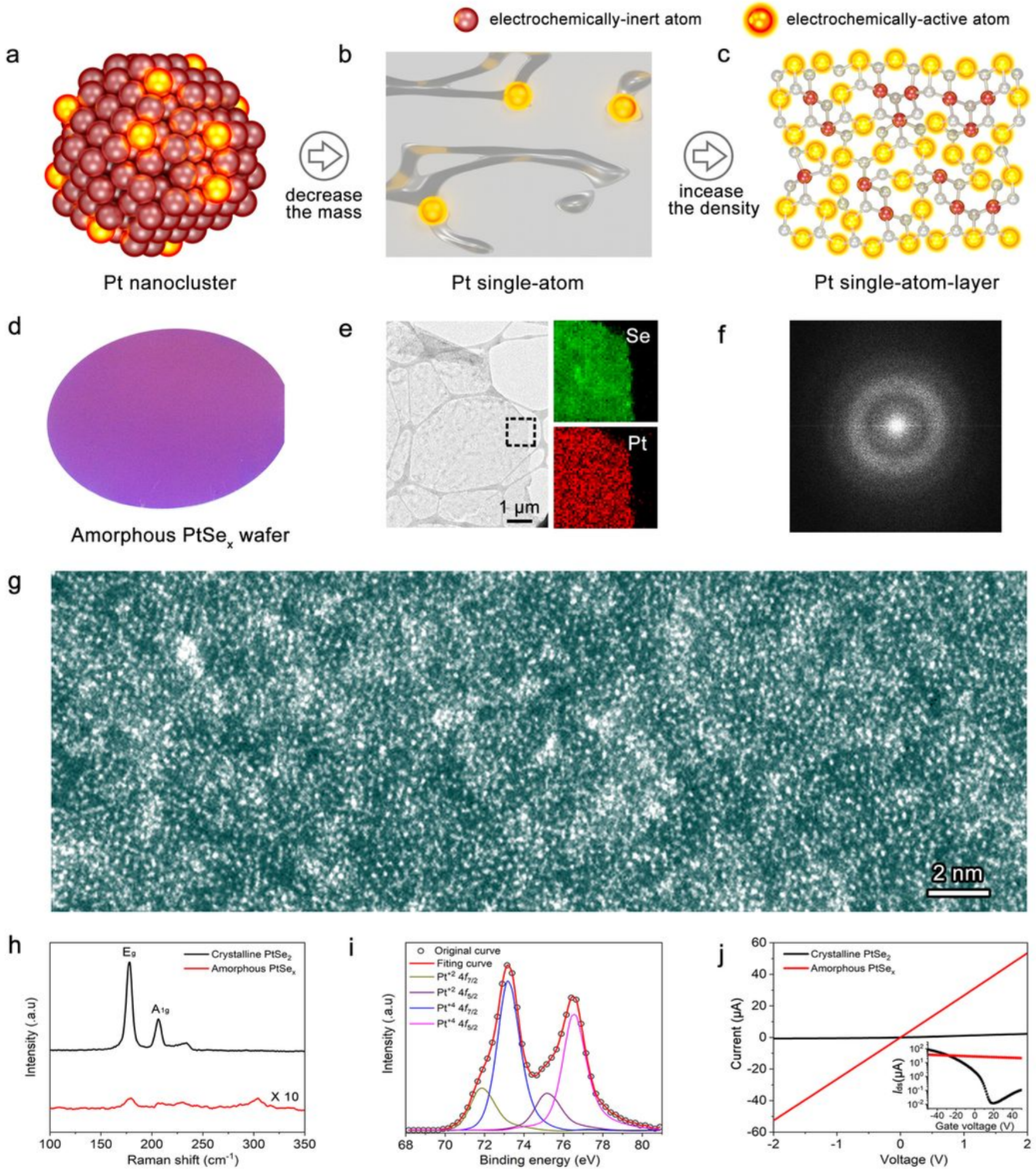

Figure 1

Pt single-atom-layer catalysis exampled by an amorphous PtSex layer. a-c, Possible structural evolution of Pt catalysts from nanocluster (a) to single-atom (b), and finally to single-atom-layer with high-density active atoms (c). d, Photograph of a 2-inch wafer of amorphous PtSex film with ~1 nm thickness. e, TEM image of a suspended PtSex amorphous film, showing its uniform, continuous, and atomically thin structure. g-f, Atomic resolution AC HAADF STEM image of an amorphous PtSex film in a large region (g)

and the typical Fourier-transform (FFT) spectrum in (f), showing a >90% ratio of amorphous regions in the whole film. h, Raman spectra of the amorphous film (below) and 1T phase of PtSe2 crystal (above). i, Pt 4f XPS spectra of the amorphous film with fitted curves, showing no significant Pt(O) peaks. j, I-V curves of amorphous PtSex and few-layer crystalline PtSe2. Inset: A back-gate field-effect transistor measurement indicates the metallic property of the amorphous PtSex.

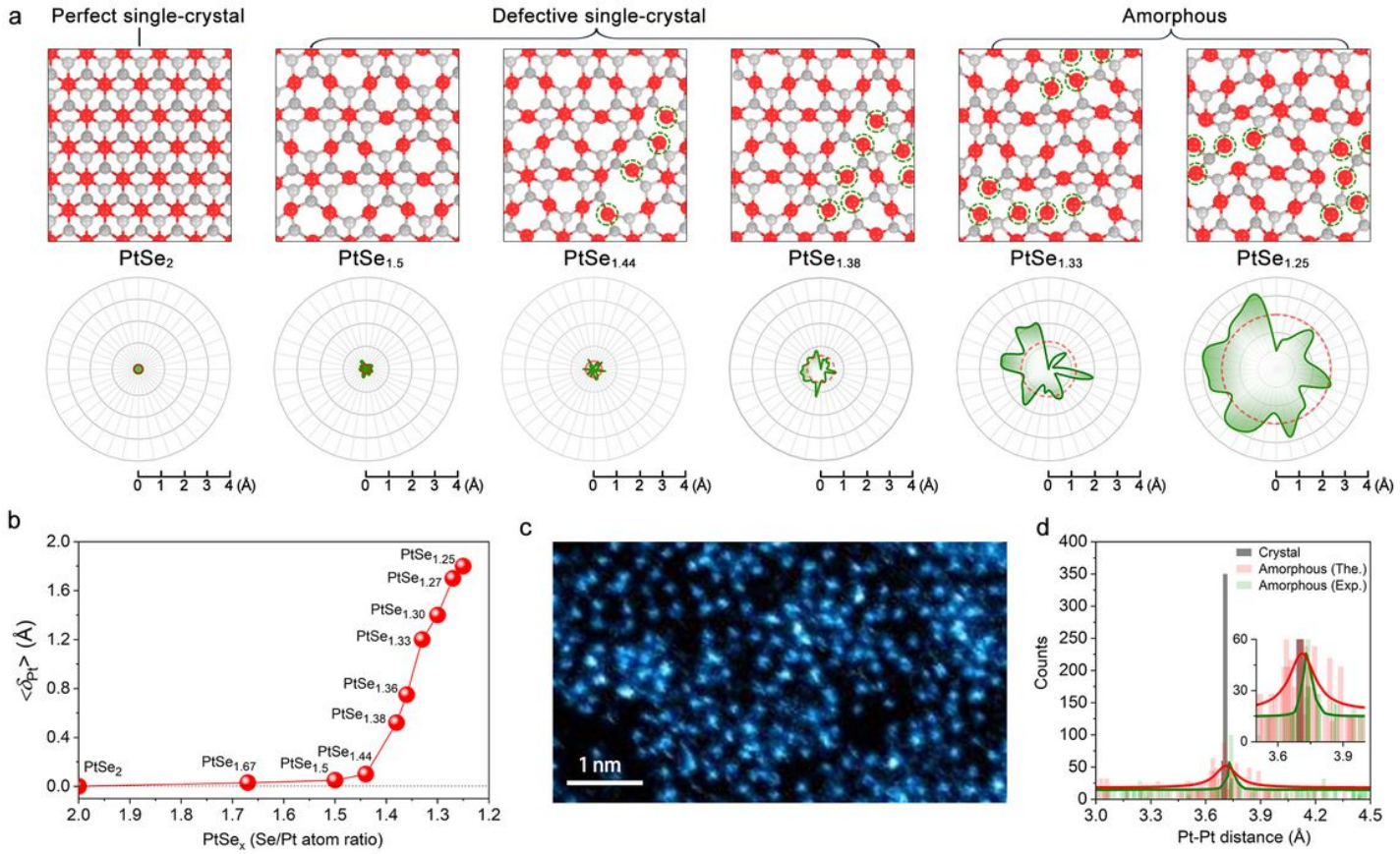

Figure 2

Formation mechanism of the 2D amorphous PtSex. a, Structural evolution of PtSex with decreasing x, obtained from ab initio molecular dynamics simulations. Top panel: atomic structures from PtSe2 to PtSex (Pt atom in red and Se atom in grey). Bottom panel: cyan line shows the displacement δPt of 36 Pt atoms (denoted by 36 radial grey lines) from their ideal positions in a PtSe2 supercell, while the red line gives the averaged displacement of all Pt atoms in PtSex, that is, <δPt>. b, <δPt> in the 2D PtSex as a function of x. An amorphous characteristic can be readily observed when x decreases to 1.38. c, Distribution of Pt atoms in a false-colored atomic resolution HAADF STEM image of an amorphous PtSex. d, Statistical distributions of the distance between two adjacent Pt-Pt atoms in an amorphous PtSex and crystalline PtSe2 monolayers.

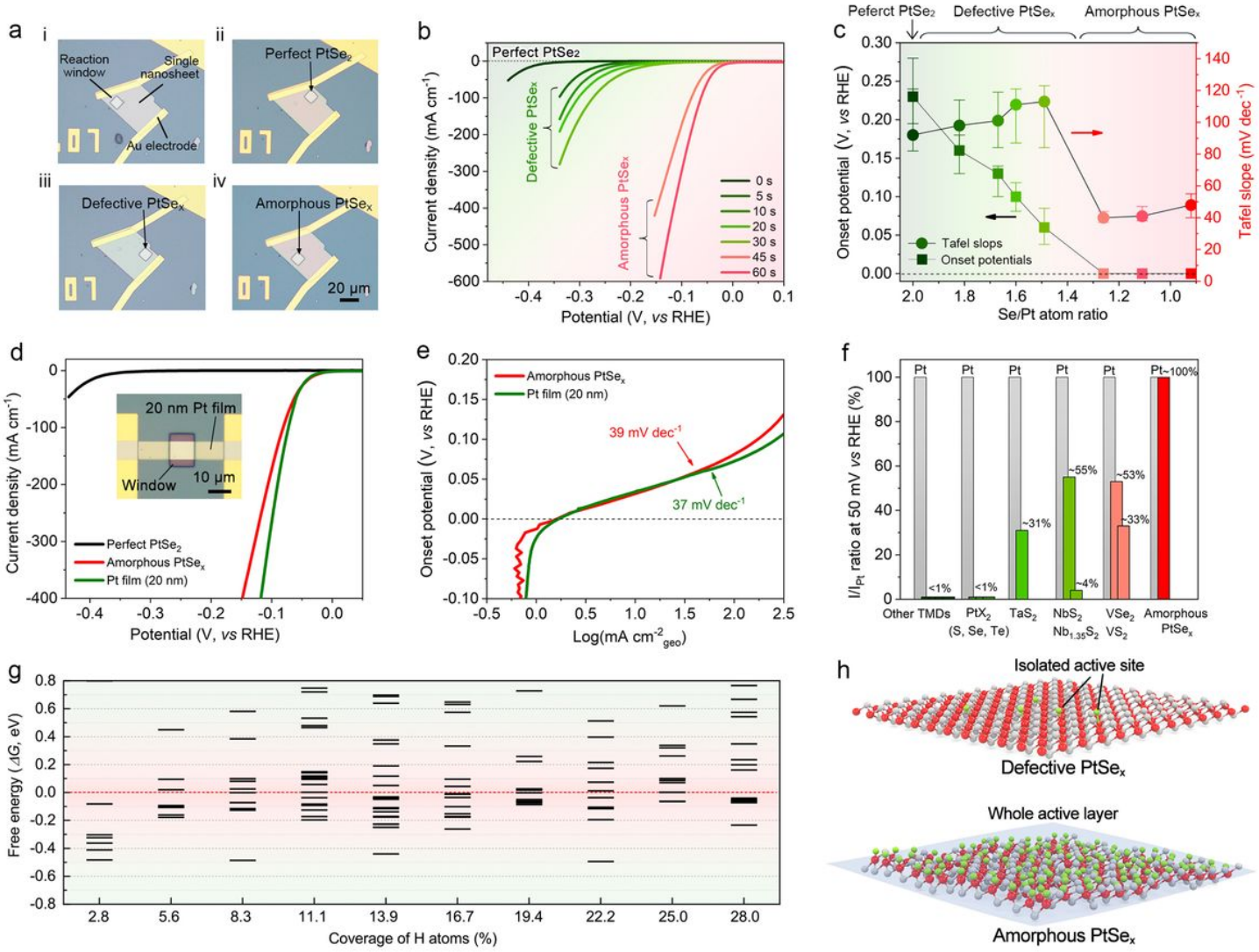

Figure 3

HER activity of amorphous PtSex catalyst by a micro-electrochemical cell. a, Optical images of PtSex microelectrodes with reaction windows. (i)-(iv) show four typical reaction windows with different plasma treatment times on a single nanosheet, where spatial control of the electrocatalytic reaction was achieved in different regions by carving windows on a passive PMMA layer. b, Polarization curves of the PtSex nanosheet with treatment duration from 0 to 60 s, corresponding to x varying from 2.0 to 1.11. c, HER catalytic activities of PtSex as a function of x, including: (i) nearly electrochemically inertness of perfect single-crystal PtSe2, (ii) moderate activity of defective single-crystal PtSex (1.3

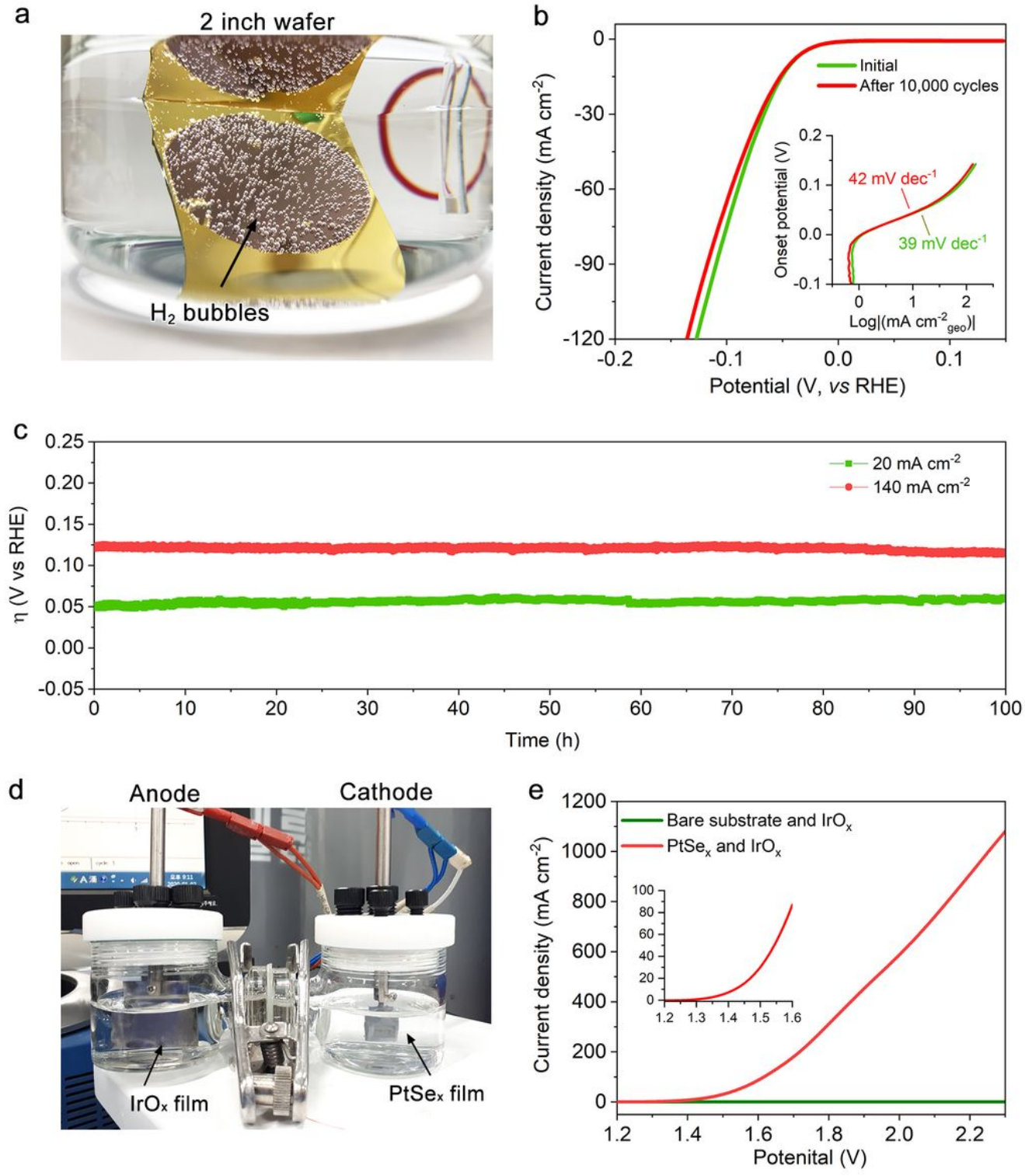

Figure 4

Wafer-scale fabrication and stability of amorphous PtSex catalyst. a, 2-inch amorphous PtSex film fabricated on an Au/SiO2/Si substrate for mass production of hydrogen gas. b, Long-term test for the amorphous PtSex, in which the polarization curves were recorded at a scan rate of 5 mV/s after 10,000 potential cycles. Inset shows the corresponding Tafel slopes. c, Time-dependent overpotential ( ) curves under j = 20 mA cm−2 and 140 mA cm−2 in 0.5 M H2SO4 aqueous solution. d, A two-electrode electrolyser

cell made of an IrOx anode and a PtSex cathode. e, Volt-ampere curves of overall water splitting in the two-electrode electrolyser.

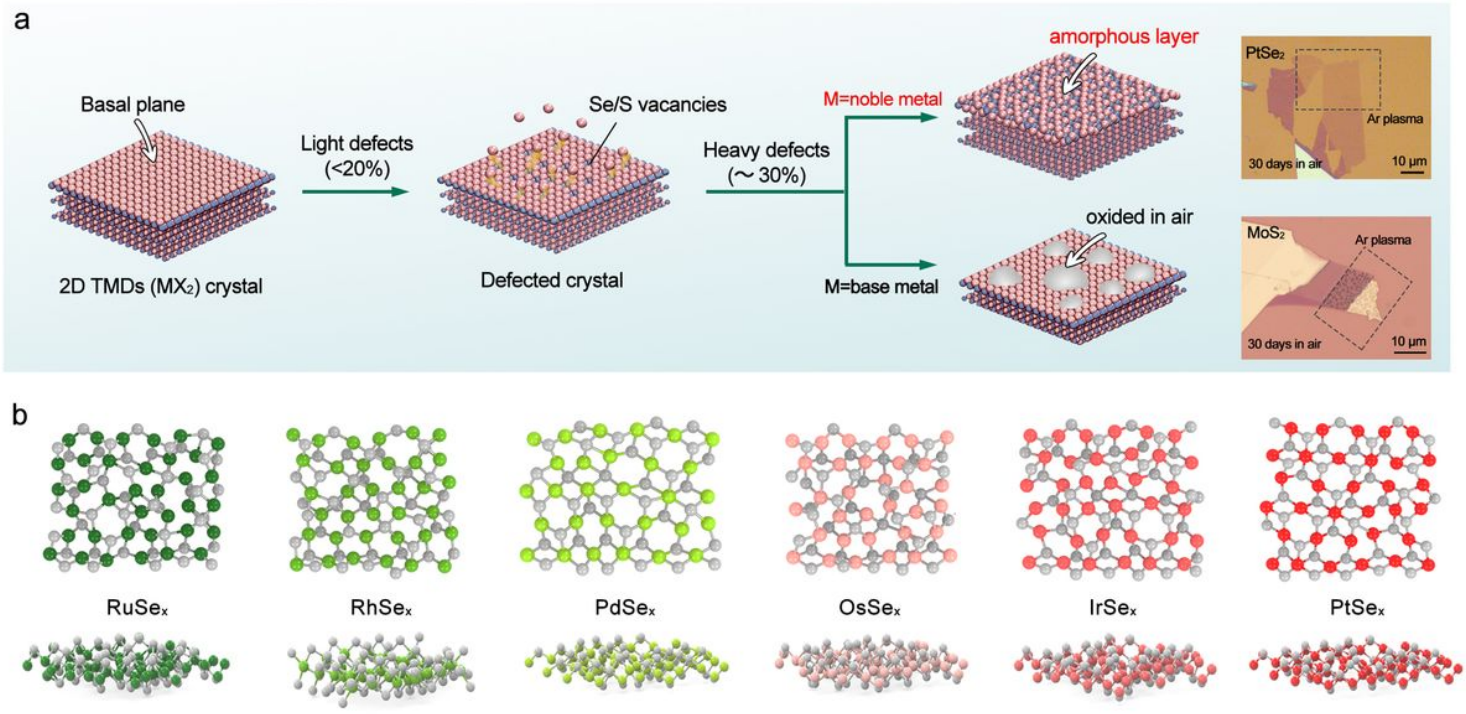

Figure 5

Possible amorphous structures in other noble metal selenides. a, Schematic of structural evolution of perfect single-crystal TMDs, showing that the amorphous structures of noble metal-based MXx (M: Pt, Pd, Ir, Os, Ru, Rh) are possibly stable in air due to resistance to corrosion and oxidation, in contrast to base metal-based MXx (M: Mo, W, Re, etc) with over-exposed M atoms readily oxidized in O2/H2O atmosphere. The optical images show distinct morphologies of MoSx and PtSex in air for 30 days after Ar plasma treatment, where small droplets exist on plasma-treated regions of MoS2. b, Possible amorphous structures obtained from ab initio molecular dynamics simulations for PtSex, PdSex, IrSex, OsSex, RuSex and RhSex (where x=1.33, Se atom in grey).

Supplementary Files

This is a list of supplementary files associated with this preprint. Click to download.

- Supplementarymovie1waferscalehydrogenproduction.mp4
- Supplementarymovie2electrolysercell.mp4
- Supportinginformation.pdf